# Multipole excitation of localized plasmon resonance in asymmetrically coated core-shell nanoparticles using optical vortices

Daisuke Tanaka[1*], Shungo Harajiri[1], Yuto Fujita[1], Kayn A. Forbes[2],
Tien Thanh Pham[3], David L. Andrews[2]


[1]Department of Electrical and Electronic Engineering, National Institute of Technology (NIT), Oita College, 1666 Maki, Oita, Japan;

[2]School of Chemistry, University of East Anglia, Norwich Research Park, Norwich, Norfolk, NR4 7TJ, U.K.;

[3]VNU Vietnam – Japan University, Vietnam National University, Hanoi, Luu Huu Phuoc Street, My Dinh 1 Ward, Nam Tu Liem District, Hanoi 100000, Vietnam;

## **Abstract**

Plasmonic interactions between an asymmetrically coated core-shell (ACCS) nanoparticle and an optical vortex produce a novel engagement of the spin angular momentum (SAM) and the orbital angular momentum (OAM) of the input. Simulations based on a discrete dipole approximation (DDA) indicate that the SAM and the OAM of the incident beam determine the modal order of resonance, correctly identifying the peak wavelength, and both the direction and magnitude of optical torque exerted upon the excited, localized plasmon resonance in the ACCS particle. These simulations also indicate higher-order resonances, including hexapole and octupole modes, and a zero-order resonance (expressible as a monopole mode), can be excited by judicious selection of the SAM and OAM. A detailed symmetry analysis shows how the multipoles associated with eigenmode excitations connect to the radiation multipoles at the heart of the multipole expansion. It is also shown how additional, distorted resonance modes due to the asymmetricity of the structure are also exhibited. These specific plasmonic characteristics, which cannot be realized by plane wave excitation, become possible through the ACCS asymmetry engaging with the distinct optical vortex nature of the excitation.

Correspondence and requests for materials should be addressed to D. T. (d-tanaka@oita-ct.ac.jp).

## Introduction

Recently, the localized plasmon resonances (LPRs) excited by structured light beams[1], such as optical vortices (OV)[2,3], have attracted attention due to their unique optical properties[4–8]. The azimuthal phase $\exp(il\phi)$ possessed by OVs leads to the electromagnetic field propagating with a helical wavefront, and the conveyance of an optical orbital angular momentum (OAM). The OAM is quantified by a topological charge $l \in \mathbb{Z}$, whose magnitude corresponds to the number of intertwined wavefront helices within a wavelength, whilst its sign designates a wavefront twist to the left $l > 0$ or right $l < 0$. Spin angular momentum (SAM), which originates from the helical path the polarization vector traces out on propagation, is quantified by a helicity $\sigma = \pm 1$ (where, for left circular polarization (LCP) $\sigma = +1$, and for right circular polarization (RCP) $\sigma = -1$). Theory for the transfer of angular momentum (AM) from the incident OV beam to the target has already been developed extensively in terms of theory based on structured beam optics and quantum mechanics[9–14]. AM transfer from light to matter can be maximized using LPRs because multipole excitation can be controlled selectively according to the total angular momentum (TAM) of the incident OV, while maintaining the benefits of the general LPR excited by a plane wave beam – such as enhancement and light confinement effect[4,5,15]. Dipole-forbidden or 'dark' multipole plasmon modes, such as the quadrupole, typically show lower radiative losses and higher quality factors than dipole modes[16,17]. Furthermore, such interactions can transfer optical AM to the structure surface and excite plasmon resonances of not only nano- but also micro-order structures[18]. Indeed, the important role that vortex beams can have in their interaction with plasmonic nanostructures is at the forefront of sensing the chirality of OV in light-matter interactions[12,14,19–22]. Therefore, LPR excitation by OV beams has a potential to pave a new path in plasmonics and chiral optics. Previous reports have focused only on two-dimensional structures such as metal nanoplates[4,5,18,23] and nanohole sub-strates[24]. To the best of our knowledge, the LPR properties of three-dimensional nanostructures (often designated 'zero-dimensional' in the field of nanotechnology) have not been reported hitherto.

The core-shell structure, in which the dielectric core particle is covered with a thin film of metal, is a typical 3D plasmonic structure which, according to the extent of surface coverage, can be sub-classified as a full-shell particle[25,26] or an asymmetrically coated core-shell (ACCS) particle (also called a Janus particle)[27–33]. The plasmonic characteristics can be tuned by the core-shell ratio and the coverage condition. In addition, since a functional component such as luminescent or non-linear optical material can be selected for the core, the structures offer highly versatile optical properties. A further advantage is that they exhibit unique optical properties due to the plasmon hybridization effect. Since this effect generally appears with the use of metal nano-multimers[7,34], these core-shell particles are attractive in that the optical characteristics derived from plasmon hybridization can be obtained with a simple single structure. In particular, the

ACCS particles, which can be fabricated in large quantities by a bottom-up method, possess particularly attractive optical characteristics associated with their asymmetricity[27–31]. As a result, ACCS particles have become key components in various optical devices such as nanolasers[32,33], nanomotors[35–37], and nano-sensors[38–40].

This paper reveals the detailed optical characteristics, including extinction spectra, resonance electric field distributions, and optical torque spectra attributed by LPRs, produced by an OV beam of RCP or LCP incident upon a ACCS 3D nanoparticle, in a simulation based on the discrete dipole approximation (DDA)[41–43]. OV beams have increasingly wide applications including photonic technologies, optical trapping, microstructure rotation in laser tweezers, chiroptical spectroscopy, and optical communication[3,14,19,44–47]. Furthermore, LPR excited by an OV beam allows those properties to be deployed in the nano-region. Our new results highlight a new degree of controllable functionality in ACCS particles, allowing for significant control of their optical properties, which is useful for designing new plasmonic devices such as plasmonic nanomotor[35–37,48].

## **Results and Discussion**

### **Extinction spectra and field distribution**

**Figure 1A** shows the model used throughout the calculations. The diameter of the core nanosphere and the thickness of the metal shell are fixed at 200 nm and 10 nm, respectively. The metal thin film of uniform thickness covers half of the nano-spheres. The core of the nanoparticle is silica, the shell gold, and the surrounding medium air. The refractive index $n$ of silica and ambient air are fixed at 1.45 and 1.0 without attenuation, ignoring dispersion. The value of the dielectric function of gold is taken from the study by Johnson and Christy[49], neglecting size dependence. In all the DDA calculations, the dipole element spacing is fixed at 2 nm.

**Figure 1B** shows the extinction spectra of a single ACCS particle excited by RCP ($\sigma = -1$) or LCP ($\sigma = +1$) OV beams with topological charges $l$ in the range from +1 to +4. The direction of incidence OV beam was set to that the wave vector $\boldsymbol{k}$ is perpendicular to the plane defined by the edge of the gold shell, as shown in Fig. 1A. The pink (LPC) and light blue (RCP) framed insets to the figure show the electric field distribution at each maximum extinction peak wavelength in the $xy$ plane at the center of the nanoparticles. In all subsequent two-dimensional electric field distribution maps, the observed planes are the cross-section thorough the center of the dielectric core particle. In most cases, the extinction spectra have two major peaks: one is a sharp peak at around 600-800 nm; the other is a broad peak around 1600 nm. Exceptionally, three major peaks arise only in the case of $l = +2$, $\sigma = -1$. This correlates with it being the only case in which the total angular momentum, TAM = OAM + SAM, is +1. Looking at the electric field distribution, the resonance mode shows the centrosymmetric multipole resonances and the order of the

resonance mode determined selectively by twice the TAM, i.e. $2\times|l + \sigma|$, without the case of monopole resonance (where TAM = 0). Therefore, in the case of positive $l$, the order of the resonance mode increases monotonically as $l$ decreases. **Table 1** summarizes the resonance mode, extinction peak wavelength, and maximum peak extinction efficiency. In the case of LCP OV beams, the excitation efficiency decreases as the order of the resonance mode increases on the short wavelength side; the opposite occurs on the long wavelength side. As for the scattering and absorption, the absorption becomes dominant, and the scattering diminishes as the order of the resonance mode increases (as shown in **Figure S1**). This tendency is consistent with the characteristics of the multipole LPR when excited by a plane-wave beam, as has been previously established[17,26]. Focusing on the peak shorter wavelengths, the maximum value of the extinction spectra decreases linearly as $l$ increases, and the resonance wavelength is blue-shifted. On the contrary, the maximum value of the longer wavelength peaks increases as $l$ increases, but the peak wavelength hardly moves. In both cases, RCP and LCP incidence, the excitation efficiencies are maximized when the quadrupole mode is excited. In this situation both the peak wavelengths are equal. However, the excitation efficiencies are not matched: the intensities are higher in the parallel case which add the AM (i.e. OAM and SAM share the same sign) than in the anti-parallel case which cancels AM. In the case of hexapole resonance excitation, the trend in the excitation efficiency is opposite to the case of quadrupole mode, but the peak wavelengths once again match. These results show that the resonance wavelength and excitation efficiency can be controlled by the OAM and the polarization degrees of freedom.

 In passing, the results of Fig. 1B exhibit fundamental principles of relevance in other, very different areas of application. When the OAM and SAM of an OV are parallel, OAM transfer to electrons in atoms and molecules cannot occur via dipole coupling under any circumstances: quadrupole or higher-order couplings are required. Furthermore, any further increase in TAM does not influence the quadrupole resonance mode. This is like the case of AM transfer in atoms and molecules wherein mismatched angular momentum is imparted to the gross motion of the matter and not the electrons[50,51].

 Before we proceed further it is important to emphasize how the multipoles associated with eigenmode excitations connect to the distinct radiation multipoles at the heart of the multipole expansion. Recent analyses by Bogdanov and co-authors are especially useful in this respect[52, 53]. The asymmetrically coated spherical nanoparticles have C∞v symmetry, for which a careful analysis of the corresponding character tables shows that the radiation engages in multipolar forms of interaction as shown in **Table 2** (see also Table A6.2 in ref 54), where En designates an electric $2^n$ multipole and Mn the corresponding magnetic $2^n$ multipole. Using lower-case Greek symbols to designate irreducible representations of the particle excitations we find, for example that to produce e2($\Delta$) excitations, quadrupolar interactions are the lowest order of effective coupling with the radiation. In the multipole

1    expansion of the interaction Hamiltonian this means coupling with electromagnetic field gradients,

2    consistent with the total angular momentum per photon. In our results, just one multipole is usually

3    dominant. Higher multipoles that might in principle be excited are not evident.

4        The results in the case of $l = +1$, $\sigma = -1$, signifying zero TAM, deserve more discussion. Under

5    this condition, a mode that can be expressed as monopole (non-polar) resonance is excited.

6    Interestingly enough, when the TAM of incident beam is zero, our simulation indicates that the

7    monopole resonance mode can be excited without AM. When a linearly polarized plane-wave

8    beam is incident (Shown in **Figure S2**), the LPR is excited by the light containing both LCP and

9    RCP components, resulting in dipole resonance. However, when a circularly polarized OV with

10   anti-parallel AM is incident, the SAM and the OAM are canceled, and a uniform enhanced electric

11   field is generated in the entire ACCP nanoparticle. Arikawa et al. experimentally[18] showed that

12   the AM of an OV transitions to a structure for a LPR phenomenon excited by a microdisk with

13   folds. However, their study was not concerned with monopole resonances. Sakai et al., who have

14   reported on OV-excited LPR in gold nanodisks[4], have shown the spectra of enhanced electric field

15   intensity at certain points on the disk surface under each incident condition. Although they have

16   not considered in detail the absorption and scattering by the entire structure, their spectra show a

17   small enhanced electric field peak under excitation conditions with zero TAM.

18       As shown in **Figure S3**, the results when $l$ is negative exhibit the same trend according to the

19   selection rule, and the same optical spectra were obtained with the combination such as of RCP

20   with $\sigma = -1$ and LCP with $\sigma = +1$. **Figure S4** shows the simulated optical spectra for the full-shell

21   particle, the optical properties are very similar to those of the ACCS particle.

22       **Figures S5 and S6** show the simulated optical spectra and electric field distributions for the

23   ACCS particle with $TiO_2$ [55] core and more high refractive material ($n = 5.0$). In the case of the

24   $TiO_2$ core, the peak wavelength is shifted to the low energy side compared to the case of an $SiO_2$

25   core. The shape of optical spectra and electric field distributions are similar to the case with $SiO_2$

26   core. When the dielectric constant of the core becomes sufficiently high that it becomes a Mie-

27   type resonance, the plasmonic properties of the ACCS particles dependent upon the structural

28   anisotropy are overshadowed, featuring modes and spectra that depend only on the state of the

29   incident OV, regardless of the direction of incidence. This result indicates that the refractive index

30   of the core material is suitable to achieve attractive optical properties from the structural

31   anisotropy of the ACCS particles.

32       **Figure 2** shows the phase dependence of the photoelectric field distribution at the resonant

33   wavelength of the ACCS nanoparticle when the RCP ($\sigma = -1$) and LCP ($\sigma = +1$) OV with $l = -1$,

34   $-2$, $-3$, and $+3$ are incident. The phase dependence can be considered equivalent in its effect to

35   the time dependence, since phase is engaged in the same complex exponential dependence as $\omega t$,

36   and the resonance mode is rotating over time with a direction determined by the sign of

1 topological charges. The intensity at the highest point is almost the same in all cases. These
2 distribution profiles cannot be seen in the case of excitation by a scalar beam. The resonance mode
3 excited by linearly polarized light is a dipole mode, and the position of each pole is fixed at all
4 times[26]. This trend is analogous to the case of gold nanodisks[4,5]. While the phase of the light wave
5 changes from 0 rad. to $\pi$ rad., the resonance electric fields of $l = -1$ to $-3$ of RCP, shown in Fig.2
6 (a), (b), and (c), rotate by $\pi/2$ rad, $\pi/3$ rad, and $\pi/4$ rad, respectively. The resonance field rotates
7 by $\pi/|l + \sigma|$ rad. For example, the angular frequency $\omega$ of the resonance mode is estimated to 1.18
8 $\times 10^{15}$ rad./sec. in the $l = -1$ case.
9 **Figure 3A** shows the extinction spectra and electric field distribution at peak wavelengths when
10 the direction of the wave vector $\boldsymbol{k}$ of the incident light and the edge of the gold nanoshell are
11 parallel. When the incident angle on the ACCS particle changes by $\pi/2$ rad. compared with case
12 of Fig. 1B, the point-symmetrical resonance modes are no longer excited. Prediction of the order
13 of resonance modes from $l$ and $\sigma$ is complicated by distorted resonance modes. Distorted dipole-
14 like or tripole-like modes are excited in the case of $l = -1$, $-2$ of RCP, and quadrupole-like or
15 hexapole-like modes in the case of $l = -3$, $-4$ of RCP. In the case of LCP, normal dipole modes
16 are excited in the case of $l = -1$, $-2$. Distorted dipole-like or tripole-like modes are excited in the
17 case of $l = -3$, $-4$. What is clear is that the order of modes tends to increase as TAM increases. In
18 both cases incident RCP and LCP, the excitation efficiency is low on both the short wavelength
19 side and the long wave-length side. In addition, as $l$ decreases, the maximum peak value on the
20 short wavelength side decreases, and the maximum peak on the long wavelength side increases.
21 There are multiple peaks both when RCP is incident and when LCP is incident, and there are cases
22 where five peaks appear as shown in the case of $l = -1$ of RCP and $l = -3$ of LCP. **Figure 3B**
23 shows the transition of resonance modes with respect to the phase change of incident light of $l =$
24 $-2$ of LCP. The position of the enhanced electric field does not change regardless of the phase of
25 the incident light, only its magnitude. This characteristic is exactly the same as that of the general
26 LPR at of linear polarized plane wave excitation, suggesting that symmetricity of the target
27 structure with respect to the incident optical electric field is required to excite multipole resonance
28 that depend on TAM.
29
30 **3D distribution of E field**
31 **Figure 4** shows a three-dimensional electric field distribution observed to confirm the overall
32 picture of the resonance field. Also shown are two-dimensional electric field distribution maps
33 and scattering profiles in the planes indicated by the red and light blue dotted lines. Against the
34 edge of the shell, the wave vector $\boldsymbol{k}$ is perpendicular in Fig. 4A and parallel in Fig. 4B, respectively.
35 $l$ and $\sigma$ were set to $-1$ and $-1$ in Fig. 4A, $-4$ and $-1$ in Fig. 4B, respectively. In the incident
36 condition of Fig. 4A, the resonance electric field is localized only at the edge of the gold shell,

1  and this distribution is very similar to the case of the full-shell particle in which the core

2  nanoparticle is fully covered with metal thin films (shown in **Figure S7**). In this case, the electric

3  field is localized in a very narrow region, and the enhancement factor at maximum is very large,

4  about three orders of magnitude. As a reflection of the distributions, the light scattering

5  characteristics are symmetrical in four directions with respect to the $xy$-plane. On the other hand,

6  under the incidence condition of Fig. 4B, the resonance field is distributed in a band shape on the

7  surface of the gold shell, and it is difficult to determine the number of resonance order from the

8  cross-sectional electric field distribution map. Rather than being localized at a specific position

9  in the nanoparticles, the electric field is widely distributed over the surface, and the enhancement

10 factor is less significant (about a factor of 10). The light scattering characteristics in this case were

11 also reflected to the electric field distributions, with light scattering asymmetrically with respect

12 to the $xy$- and $xz$-planes, re-radiation being stronger in areas with stronger electric fields. When a

13 ring-shaped resonance mode is excited, whose order of LPR mode is predictable from the TAM

14 as in Fig. 4A, the electric field rotates with time. On the other hand, when a distorted LPR mode

15 is excited, as in Fig. 4B, its electric field does not rotate with time, but the electric field is unevenly

16 localized in a band in only certain part of the particle surface. Therefore, this three-dimensional

17 electric field distribution diagram easily leads us to imagine that the LPR generates a rotational

18 torque on this ACCS nanoparticles. Moreover, the torque is generated to the three-dimensional

19 direction. This is because we know that both the rotation of the electric field and the bias of the

20 electric field generated the optical torques.

21 **Optical torque spectra**

22   **Figure 5** shows both the excitation spectra and torque efficiency spectra of the ACCS particle

23 in water ($n = 1.33$) against axes, $x$, $y$, and, $z$ at each rotation angle. The linearly polarized OV

24 beam of $l = +1$ is incident with the geometry shown in Fig. 1A. The extinction peak derived from

25 LPR excited by the linearly polarized OV gives the equivalent result to that given by combining

26 the results of excitation by RCP and LCP beams. The extinction peaks derived from LPR excited

27 by LCP and RCP appear near 900 nm and 1300 nm, respectively. When the refractive index of

28 the ambient medium becomes high, the peak wavelength is different from the extinction spectrum

29 shown in Fig. 1B due to the red shift similar to that of general LPR. Similar to the extinction

30 spectra, the torque spectra for the $z$-axis shown in Fig. 5D also show positive (counterclockwise)

31 and negative (clockwise) peaks near 900 nm and 1300 nm. From this, it emerges that the optical

32 torque with respect to the $z$-axis is strongly related to the extinction spectra, and it is suggested

33 that the generated torque depends on the polarization condition of the incident OV beam. **Figure**

34 **S8** shows the torque spectra excited by RCR and LCP OV beams. The trends in the torque spectra

35 in the case of $l = +2$, and $+3$ are similar to the case of $l = +1$ (shown in **Figure S9**). It was found

36 that the torque characteristics can be selected by $l$ as well as the extinction characteristics. On the

other hand, the torque spectra for the $x$-axis and $y$-axis shown in Fig. 5B and 5C are not related to the extinction spectra such as the torque for the $z$-axis. These characteristics display an anti-symmetry between the first two and second two quadrants, i.e., 0° to 180° and 180° to 360°, and even if the incident direction of light with respect to the nanostructure is opposite, the direction and intensity of rotational torque are no difference. In these results, the LPR excited by the OV generates rotational torque of the same magnitude with respect to the three-dimensional axes, and its intensity and direction can be selectively controlled by wavelength, degree of polarization, and $l$ of incident light source.

## Conclusion

In conclusion, our numerical simulations have revealed the LPR properties of 3D ACCS nanoparticles excited by OV beams carrying optical OAM. The key advantage of OVs over plane waves is their three-dimensional spatial structure in phase and amplitude, offering an additional degree of freedom. OVs convey larger field gradients (due to their ring-like amplitude profile and azimuthal phase) than a Gaussian beam, for example. Due to the highly structured nature of OVs, the associated larger field gradients lead to the advantages of tailored multipole excitation exemplified by our studies.

It has been shown that the peak wavelength and shape of extinction spectra change according to the beam parameters $l$ and $\sigma$, which corresponds to OAM and SAM, in the direction of incident light. When the excited LPR mode is symmetric, that is determined by selection rules of TAM and that rotates over time. However, in the case that the mode is disordered, the expectation of the resonance mode from TAM does not hold. Our calculation has also shown that the LPR of the ACCS particle generates a torque against the axis of cylindrical symmetry. These results on the LPR showed that the optical properties of ACCS particles with possibility of adding functionality can be controlled in the same way as metal nanodisks and microplates – a feature that is useful for designing new plasmonic devices such as plasmonic nanomotor. The efficient and controllable transfer of both OAM and TAM from light to materials used in solid-state devices affords a foundation for novel photonic devices exploiting OAM light.

## Numerical Calculations

We numerically calculated the electromagnetic field, optical spectra, light scattering profiles, and torque spectra in our system by using the DDSCAT 7.3[41–43] software with partly rewritten calculation codes. The DDSCAT describes the state of the polarization of the incident light by Jones calculus. The polarization condition of the incident scalar beam in DDSCAT can be entered in ddscat.par with or without real and imaginary parts of electric field components in the x- and y- directions. The electric field can be expressed by the following Jones vector:

$$\mathsf{J} = \frac{1}{\sqrt{\mathsf{E}_{x0}^2 + \mathsf{E}_{y0}^2}} \begin{pmatrix} \mathsf{E}_{x0} \\ \mathsf{E}_{y0}\exp(-i\delta) \end{pmatrix}$$

1

$$\xrightarrow{\cos\beta = \frac{\mathsf{E}_{x0}}{\sqrt{\mathsf{E}_{x0}^2+\mathsf{E}_{y0}^2}},\, \sin\beta = \frac{\mathsf{E}_{y0}}{\sqrt{\mathsf{E}_{x0}^2+\mathsf{E}_{y0}^2}}} \mathsf{J} = \begin{pmatrix} \cos\beta \\ \sin\beta\cos\delta - i\sin\beta\sin\delta \end{pmatrix} \qquad (1)$$

2     where $\mathsf{E}_{x0}$ and $\mathsf{E}_{y0}$ are the amplitude of the two components of the electric field vector, while $\delta$ is the

3     phase difference of the two components of the vector. In the OV case, the phase is different at each

4     location in the calculation space, so that the state of the optical field differs depending on the location

5     of each dipole. With the position $\mathsf{x}$, $\mathsf{y}$ of each dipole, we express the azimuth angle $\phi$ of the electric

6     field oscillating in the $\mathsf{xy}$ plane.

7

$$\phi = \arg(\mathsf{x},\mathsf{y}) = \mathrm{atan2}(\mathsf{y},\mathsf{x}) \qquad (2)$$

8     And using this angle $\phi$ calculated by the function datan2 in Fortran90 to express the $\mathsf{J}$ of OV,

9

$$\mathsf{J} = \begin{pmatrix} \mathsf{E}_x \\ \mathsf{E}_y \end{pmatrix} = \frac{e^{-il\phi}}{\sqrt{2}} \begin{pmatrix} 1 \\ i \end{pmatrix} \qquad (3)$$

10     where is the, $i$ is the imaginary unit in the case that the incident light propagates in the $z$ direction, and

11     $l$ is the topological charge[56, 57]. The electric field component in the direction of propagation $\mathsf{E}_z$ is

12     assumed to be zero. Here, $\phi$ is the azimuth angle after passing through an axisymmetric polarizing

13     element such as a $q$-plate. What this means is that equation (3) is obtained as a result of the combination

14     of optical elements required to experimentally generate the OV acting as a Jones matrix. This equation

15     expresses the LCP OV, and it can be changed to RCP light by changing the sign of $\mathsf{y}$ components. The

16     vortex beam of RCP, LCP, and liner polarization is set as the incident light with $l = \pm1, \pm2, \pm3,$ and $\pm4$.

17     The following equation (4) express the linear OV with $l$.

18

$$\mathsf{J} = \begin{pmatrix} \mathsf{E}_x \\ \mathsf{E}_y \end{pmatrix} = e^{-il\phi} \begin{pmatrix} 0 \\ 1 \end{pmatrix} \qquad (4)$$

19     The DDSCAT software can calculate the complex scattering matrix $\mathsf{f}_{mn}(\theta,\varphi)$, where the index $\mathsf{n} =$

20     $1, 2$ denotes the incident polarization state, $\mathsf{m} = 1, 2$ denotes the scattered polarization state, $\theta$ specifies

21     the scattering angle between incident axis and $\mathsf{y}$ axis, and $\varphi$ specifies the scattering angle which in the

22     plane perpendicular to the $\theta$ direction. For example, when $\theta = 0$ ($\theta$ direction coincides with $z$, the

23     direction in which the light propagates), $\varphi$ represents the scattering angle in the $\mathsf{xy}$-plane; when $\theta =$

24     $\pi/2$ ($\theta$ direction coincides with the $\mathsf{y}$-axis), $\varphi$ represents the scattering angle in the $\mathsf{xz}$-plane. As our

25     computational conditions were invariably only one polarization state, the only component of this

26     scattering matrix is $\mathsf{n}=1$, and the scattering cross section $\mathsf{C}_{sca}$ for each angle can be expressed as in the

27     equation below.

$$\left(\frac{dC_{sca}}{d\varphi}\right)_{\theta=0} = \frac{1}{k^2}\left|f_{11}\right|^2 \tag{4}$$

$$\left(\frac{dC_{sca}}{d\varphi}\right)_{\theta=\pi/2} = \frac{1}{k^2}\left|f_{21}\right|^2 \tag{5}$$

In Fig. 4, the maximum value of the square of the elements of the scattering matrix $|f_{11}|^2$ and $|f_{21}|^2$ is normalized to 1 and shown in polar plots.

We observed the extinction spectra, the torque spectra, and the electric field distribution of ACCS particles at peak wavelengths. The torque efficiency is calculated by the following equation (6) by DDSCAT.

$$Q_{\Gamma} = \frac{k\Gamma_{rad}}{\pi a_{eff}^2 u_{rad}} \tag{6}$$

where $\Gamma_{rad}$ is time averaged torque, $k$ is the wave vector, $a_{eff}$ is the effective radius, and $u_{rad}$ is the time average energy density for an incident wave with amplitude $E_0 = 1$ V m$^{-1}$. The dipole element spacing of the calculation models was set to 2 nm in all cases.

## **Associated Content**

Ⓢ  Supporting Information

The Supporting Information is available free.

Figure S1-S4: Optical spectra of single ACCS particle for OV beam or linear plane wave beam with different beam conditions. Figure S5, S6: Extinction spectra and electric field distribution of single full-shell particle for OV beams.    Figure S7, S8: Optical torque spectra of single ACCS particle for OV with different beam conditions.

## **Author Contributions:**

D. T planned and designed the study. D. T., S. H, and Y. F. obtained the simulated data. D. T., S. H., Y. F., K. A. F., T. T. F., and D. L. A. performed data analysis. D. T., K. A. F., and D. L. A. co-wrote the manuscript.

## **Funding Sources**

## **Abbreviations**

ACCS; Asymmetrically Coated Core-Shell; LPR, Localized Plasmon Resonance; SAM, Spin Angular

Momentum; OAM, Orbital Angular Momentum; TAM, Total Angular Momentum; DDA, Discrete Dipole Approximation.

## **References**

1. Forbes, A.; de Oliveira, M.; Dennis, M. R. Structured Light. *Nature Photonics* **2021**, *15* (4), 253–262.

2. Huang, L.; Song, X.; Reineke, B.; Li, T.; Li, X.; Liu, J.; Zhang, S.; Wang, Y.; Zentgraf, T. Volumetric Generation of Optical Vortices with Metasurfaces. *ACS Photonics* **2017**, *4* (2), 338–346.

3. Shen, Y.; Wang, X.; Xie, Z.; Min, C.; Fu, X.; Liu, Q.; Gong, M.; Yuan, X. Optical Vortices 30 Years on: OAM Manipulation from Topological Charge to Multiple Singularities. *Light: Science & Applications* **2019**, *8* (1), 1–29.

4. Sakai, K.; Nomura, K.; Yamamoto, T.; Sasaki, K. Excitation of Multipole Plasmons by Optical Vortex Beams. *Scientific Reports* **2015**, *5* (1), 8431.

5. Harajiri, S.; Tanaka, D. Discrete Dipole Approximation Simulation of LPR Properties of Single Metal Nanodisk Excited by Optical Vortex Beam. *Transaction of the Japan Society for Simulation Technology* **2020**, *12* (1), 21–27.

6. Lehmuskero, A.; Li, Y.; Johansson, P.; Käll, M. Plasmonic Particles Set into Fast Orbital Motion by an Optical Vortex Beam. *Optics Express* **2014**, *22* (4), 4349–4356.

7. Hentschel, M.; Dorfmüller, J.; Giessen, H.; Jäger, S.; Kern, A. M.; Braun, K.; Zhang, D.; Meixner, A. J. Plasmonic Oligomers in Cylindrical Vector Light Beams. *Beilstein Journal of Nanotechnology* **2013**, *4* (1), 57–65.

8. Prinz, E.; Hartelt, M.; Spektor, G.; Orenstein, M.; Aeschlimann, M. Orbital Angular Momentum in Nano-plasmonic Vortices. *ACS Photonics* **2023**, *10* (2), 340–367.

9. Zambrana-Puyalto, X.; Vidal, X.; Molina-Terriza, G. Excitation of Single Multipolar Modes with Engineered Cylindrically Symmetric Fields. *Optics Express* **2012**, *20* (22), 24536–24544.

10. Babiker, M.; Andrews, D. L.; Lembessis, V. E. Atoms in Complex Twisted Light. *Journal of Optics* **2018**, *21* (1), 013001.

11. Forbes, K. A.; Andrews, D. L. Optical Orbital Angular Momentum: Twisted Light and Chirality. *Optics Letters* **2018**, *43* (3), 435–438.

12. Reddy, I. V.; Baev, A.; Furlani, E. P.; Prasad, P. N.; Haus, J. W. Interaction of Structured Light with a Chiral Plasmonic Metasurface: Giant Enhancement of Chiro-Optic Response. *ACS Photonics* **2018**, *5* (3), 734–740.

13. Spektor, G.; Kilbane, D.; Mahro, A. K.; Frank, B.; Ristok, S.; Gal, L.; Kahl, P.; Podbiel, D.; Mathias, S.; Giessen, H. Revealing the Subfemtosecond Dynamics of Orbital Angular Momentum in Nanoplasmonic Vortices. *Science* **2017**, *355* (6330), 1187–1191.

14. Porfirev, A.; Khonina, S.; Kuchmizhak, A. Light–Matter Interaction Empowered by Orbital Angular Momentum: Control of Matter at the Micro- and Nanoscale. *Progress in Quantum Electronics* **2023**, 100459. https://doi.org/10.1016/j.pquantelec.2023.100459.

15. Hentschel, M.; Schäferling, M.; Duan, X.; Giessen, H.; Liu, N. Chiral Plasmonics. *Science Advances* **2017**, *3* (5), e1602735.

16. Zhang, S.; Bao, K.; Halas, N. J.; Xu, H.; Nordlander, P. Substrate-Induced Fano Resonances of a Plasmonic Nanocube: A Route to Increased-Sensitivity Localized Surface Plasmon Resonance Sensors Revealed. *Nano Letters* **2011**, *11* (4), 1657–1663.

17. Wei, X. Z.; Mulvaney, P. Optical Properties of Strongly Coupled Plasmonic Nanoparticle Clusters. In *Handbook of surface science*; Elsevier, 2014; Vol. 4, pp 75–108.

18. Arikawa, T.; Hiraoka, T.; Morimoto, S.; Blanchard, F.; Tani, S.; Tanaka, T.; Sakai, K.; Kitajima, H.; Sasaki, K.; Tanaka, K. Transfer of Orbital Angular Momentum of Light to Plasmonic Excitations in Metamaterials. *Science Advances* **2020**, *6* (24), eaay1977.

19. Forbes, K. A.; Andrews, D. L. Orbital Angular Momentum of Twisted Light: Chirality and Optical Activity. *J. Phys. Photonics* **2021**, *3* (2), 022007.

20. Woźniak, P.; Leon, I. D.; Höflich, K.; Leuchs, G.; Banzer, P. Interaction of Light Carrying Orbital Angular Momentum with a Chiral Dipolar Scatterer. *Optica* **2019**, *6* (8), 961–965.

21. Green, D.; Forbes, K. A. Optical Chirality of Vortex Beams at the Nanoscale. *Nanoscale* **2023**, *15* (2), 540–552.

22. Forbes, K. A.; Jones, G. A. Optical Vortex Dichroism in Chiral Particles. *Phys. Rev. A* **2021**, *103* (5), 053515.

23. Sakai, K.; Yamamoto, T.; Sasaki, K. Nanofocusing of Structured Light for Quadrupolar Light-Matter Interactions. *Scientific Reports* **2018**, *8* (1), 7746.

24. Sakai, K.; Nomura, K.; Yamamoto, T.; Omura, T.; Sasaki, K. Quadrupole Lattice Resonances in Plasmonic Crystal Excited by Cylindrical Vector Beams. *Scientific Reports* **2016**, *6* (1), 34967.

25. Prodan, E.; Radloff, C.; Halas, N. J.; Nordlander, P. A Hybridization Model for the Plasmon Response of Complex Nanostructures. *Science* **2003**, *302* (5644), 419–422.

26. Prasad, P. N. *Nanophotonics*; John Wiley & Sons, 2004.

27. Fujimura, R.; Zhang, R.; Kitamoto, Y.; Shimojo, M.; Kajikawa, K. Modeling of Semi-Shell Nanostructures Formed by Metal Deposition on Dielectric Nanospheres and Numerical Evaluation of Plasmonic Properties. *Japanese Journal of Applied Physics* **2014**, *53* (3), 035201.

28. Matsumori, K.; Fujimura, R. Thermal Stability and Optical Properties of an Al Semishell Nanostructure. *Optical Materials Express* **2018**, *8* (5), 1265–1273.

29. Scherbak, S.; Kapralov, N.; Reduto, I.; Chervinskii, S.; Svirko, O.; Lipovskii, A. Tuning Plasmonic Properties of Truncated Gold Nanospheres by Coating. *Plasmonics* **2017**, *12*, 1903–1910.

30. Zhang, Y.; Grady, N. K.; Ayala-Orozco, C.; Halas, N. J. Three-Dimensional Nanostructures as Highly Efficient Generators of Second Harmonic Light. *Nano Letters* **2011**, *11* (12), 5519–5523.

31. Cortie, M.; Ford, M. A Plasmon-Induced Current Loop in Gold Semi-Shells. *Nanotechnology* **2007**, *18* (23), 235704.

32. Meng, X.; Guler, U.; Kildishev, A. V.; Fujita, K.; Tanaka, K.; Shalaev, V. M. Unidirectional Spaser in Symmetry-Broken Plasmonic Core-Shell Nanocavity. *Scientific Reports* **2013**, *3* (1), 1241.

33. Wang, R.; Xu, C.; You, D.; Wang, X.; Chen, J.; Shi, Z.; Cui, Q.; Qiu, T. Ultra-Strong Mode Confinement at Semishell Metal/Insulator/Semiconductor Interface for Nanolaser. *Journal of Luminescence* **2021**, *238*, 118242.

34. Yang, S.-C.; Kobori, H.; He, C.-L.; Lin, M.-H.; Chen, H.-Y.; Li, C.; Kanehara, M.; Teranishi, T.; Gwo, S. Plasmon Hybridization in Individual Gold Nanocrys-tal Dimers: Direct Observation of Bright and Dark Modes. *Nano Letters* **2010**, *10* (2), 632–637.

35. Xu, L.; Mou, F.; Gong, H.; Luo, M.; Guan, J. Light-Driven Micro/Nanomotors: From Fundamentals to Applications. *Chemical Society Reviews* **2017**, *46* (22), 6905–6926.

36. Zheng, J.; Lam, S. H.; Huang, H.; Shao, L. Recent Progress in Optical-Resonance-Assisted Movement Control of Nanomotors. *Advanced Intelligent Systems* **2020**, *2* (3), 1900160.

37. Ilic, O.; Kaminer, I.; Zhen, B.; Miller, O. D.; Buljan, H.; Soljačić, M. Topologically Enabled Optical Nanomotors. *Science Advances* **2017**, *3* (6), e1602738.

38. Endo, T.; Kerman, K.; Nagatani, N.; Hiepa, H. M.; Kim, D.-K.; Yonezawa, Y.; Nakano, K.; Tamiya, E. Multiple Label-Free Detection of Antigen- Antibody Reaction Using Localized Surface Plasmon Resonance-Based Core- Shell Structured Nanoparticle Layer Nanochip. *Analytical Chemistry* **2006**, *78* (18), 6465–6475.

39. Himmelhaus, M.; Takei, H. Cap-Shaped Gold Nano-particles for an Optical Biosensor. *Sensors and Actuators B: Chemical* **2000**, *63* (1–2), 24–30.

40. Szunerits, S.; Spadavecchia, J.; Boukherroub, R. Surface Plasmon Resonance: Signal Amplification Using Colloidal Gold Nanoparticles for Enhanced Sensitivity. *Reviews in Analytical Chemistry* **2014**, *33* (3), 153–164.

41. Draine, B. T.; Flatau, P. J. Discrete-Dipole Approximation for Scattering Calculations. *J. Opt. Soc. Am. A* **1994**, *11* (4), 1491–1499.

42. Draine, B. T.; Flatau, P. J. Discrete-Dipole Approximation for Periodic Targets: Theory and Tests. *J. Opt. Soc. Am. A* **2008**, *25* (11), 2693–2703.

43. Flatau, P. J.; Draine, B. T. Fast near Field Calculations in the Discrete Dipole Approximation for Regular Rectilinear Grids. *Optics Express* **2012**, *20* (2), 1247–1252.

44. *Structured Light and Its Applications: An Introduction to Phase-Structured Beams and Nanoscale Optical Forces*; Andrews, D. L., Ed.; Academic press: Burlington, 2011.

45. *The Angular Momentum of Light*; Andrews, D. L., Babiker, M., Eds.; Cambridge University

Press: Cambridge, 2012.

46. Yang, Y.; Ren, Y.; Chen, M.; Arita, Y.; Rosales-Guzmán, C. Optical Trapping with Structured Light: A Review. *Advanced Photonics* **2021**, *3* (3), 034001.

47. Simbulan, K. B.; Feng, Y.-J.; Chang, W.-H.; Lu, C.-I.; Lu, T.-H.; Lan, Y.-W. Twisted Light-Enhanced Photo-voltaic Effect. *ACS Nano* **2021**, *15* (9), 14822–14829.

48. Tanaka, Y. Y.; Albella, P.; Rahmani, M.; Giannini, V.; Maier, S. A.; Shimura, T. Plasmonic Linear Nanomotor Using Lateral Optical Forces. *Science Advances* **2020**, *6* (45), eabc3726.

49. Johnson, P. B.; Christy, R. W. Optical Constants of the Noble Metals. *Physical Review B* **1972**, *6* (12), 4370.

50. Babiker, M.; Bennett, C. R.; Andrews, D. L.; Romero, L. D. Orbital Angular Momentum Exchange in the Interaction of Twisted Light with Molecules. *Physical Review Letters* **2002**, *89* (14), 143601.

51. Schmiegelow, C. T.; Schulz, J.; Kaufmann, H.; Ruster, T.; Poschinger, U. G.; Schmidt-Kaler, F. Transfer of Optical Orbital Angular Momentum to a Bound Electron. *Nature Communications* **2016**, *7*, 12998.

52. Poleva, M.; Frizyuk, K.; Baryshnikova, K.; Evlyukhin, A.; Petrov, M.; Bogdanov, A. Multipolar theory of bianisotropic response of meta-atoms. *Physical Review B* **2023**, *107*, L041304.

53. Gladyshev, S.; Frizyuk, K.; Bogdanov, A. Symmetry analysis and multipole classification of eigenmodes in electromagnetic resonators for engineering their optical properties. *Physical Review B* **2020**, *102*, 075103.

54. *Optical Harmonics in Molecular Systems*; Andrews, D. L. and Allcock, P.; Wiley-VCH, Weinheim, 2002.

55. Devore, J. R. Refractive Indices of Rutile and Sphalerite. *J. Opt. Soc. Am*, **1951**, *41*, 416-419.

56. Marrucci L.; Manzo C.; Paparo D. Optical Spin-to-Orbital Angular Momentum Conversion in Inhomogeneous Anisotropic Media. *Physical Review Letters*, **2006**, *96*, 163905.

57. Tokizane Y.; Oka K.; Morita R. Supercontinuum optical vortex pulse generation without spatial or topological-charge dispersion. *Optics Express*, **2009**, *17*, 14517-14525.

1 **Figure 1**

2 A: Geometry of the calculation model. B: Simulated extinction spectra and momentary electric field

3 distribution of single ACCS particle for RCP ($\sigma = -1$) and LCP ($\sigma = +1$) OV beams with different $l$,

4 incident from a direction in which the wave vector $\boldsymbol{k}$ is perpendicular to the $xy$ plane containing the

5 edge of the gold shell. The observed planes of the field distributions are the $xy$-plane through the center

6 of the core particle.

7

8 **Table 1**

9 Resonance mode, maximum extinction peak wavelength, and the efficiency for each excited OV

10 condition ($\sigma = \pm 1$, $l = +1, +2, +3, +4$).

11

12 **Table 2**

13 Symmetries and irreducible representations of normal mode excitations in axially excited C∞v

14 particles and the radiation multipoles through their excitations are allowed.    For clarity the irreducible

15 representation labels are written in lower-case with spectroscopic (Greek) equivalents: En designates

16 an electric $2^n$ multipole and Mn the corresponding magnetic $2^n$ multipole.

17

18 **Figure 2**

19 Transition of resonance modes with respect to the phase change of incident light. The values of $l$ are:

20 (a) −1, (b) −2, (c) −3, and (d), (e) +3; for (a-d) $\sigma = -1$, and for (e) $\sigma = +1$. The direction of the wave

21 vector $\boldsymbol{k}$ is perpendicular to the edge of the shell of the ACCS nanoparticle. The observed planes of

22 the field distributions are the $xy$-plane through the center of the core particle.

23

24 **Figure 3**

25 A. Simulated extinction spectra and momentary electric field distribution of single ACCS particle for

26 RCP ($\sigma = -1$) and LCP ($\sigma = +1$) OV beams with different $l$, incident in the direction such that the wave

27 vector $\boldsymbol{k}$ is parallel to the metal nanoshell. B. Transition of resonance modes with respect to the phase

28 change of incident light of $l = -2$ of LCP. The observed planes of the field distributions are the $xy$-

29 plane through the center of the core particle.

30

31

32 **Figure 4**

33 2D and 3D electric field distributions of single ACCS particle in the case that the OV beam of A.

34 RCP with $l = -1$ at 775 nm and B. RCP with $l = -4$ at 550 nm is incident with different directions,

35 A. parallel and B. perpendicular to the edge of the gold shell. The observed planes of the field

36 distributions are the $xy$- and $xz$-planes through the center of the core particle. The normalized polar

1  plot diagrams in the same plane to the 2D electric field distributions are shown to the scattering

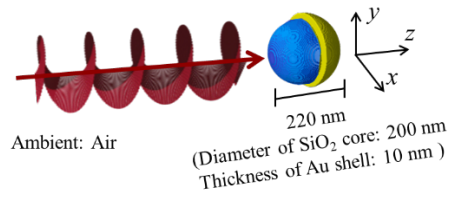2  properties from $f_{11}{}^2$ and $f_{21}{}^2$.

3

4  **Figure 5**

5  A. Extinction spectra of the ACCS particle in water at each rotation angle. B. C. D. Optical torque

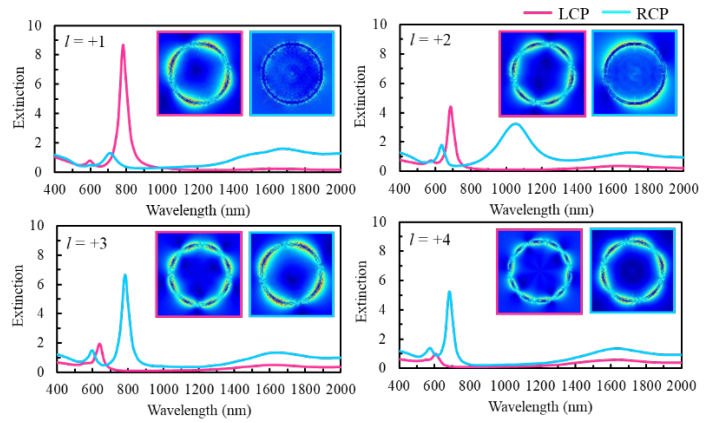6  spectra against $x$, $y$, and $z$ axes, respectively.

7

8

9

10

11

12

13

14

15

16

17

18

19

20

21

22

23

24

25

26

27

28

29

30

31

32

33

34

35

36

A

Topological charge $l$ : $\pm 1$, $\pm 2$, $\pm 3$, $\pm 4$

Polarization: RCP($\sigma = -1$), LCP($\sigma = +1$)

Ambient: Air

220 nm
(Diameter of SiO$_2$ core: 200 nm
Thickness of Au shell: 10 nm )

B



D. Tanaka et al. Figure 1

| σ \ $l$ | 0 (scalar) | +1 | +2 | +3 | +4 |
|---|---|---|---|---|---|
| +1 | Dipole 1060 nm 7.27 | Quadrupole 782 nm 8.67 | Hexapole 686 nm 4.43 | Octupole 638 nm 1.96 | Decapole 608 nm 0.97 |
| −1 | Dipole 1060 nm 7.27 | Non-pole 1675 nm 1.60 | Dipole 1054 nm 3.23 | Quadrupole 782 nm 6.65 | Hexapole 686 nm 5.23 |

D. Tanaka et al. Table 1

1
2
3
4
5
6
7
8
9
10
11
12
13
14
15
16
17
18
19
20
21
22
23
24
25
26
27

| Excitations | Radiation multipoles allowed |
|---|---|
| a1($\Sigma^+$) | E1, E2, E3 and M2, M3 |
| a2($\Sigma^-$) | E2, E3 and M1, M2, M3 |
| e1($\Pi$) | E1, E2, E3 and M1, M2, M3 |
| e2($\Delta$) | E2, E3 and M2, M3 |
| e3($\Phi$) | E3 and M3 |

1

2    D. Tanaka et al. Table 2

3

4

5

6

7

8

9

10

11

12

13

14

15

16

17

18

19

20

21

22

23

24

25

26
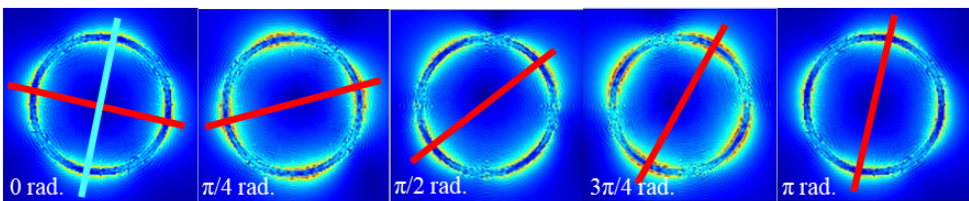
27

28

29

30

(a) RCP ($\sigma = -1$), $l = -1$ @782 nm

$$\left|\frac{\mathrm{Re}(\boldsymbol{E})}{E_o}\right|^2$$

Max

0 rad.    π/4 rad.    π/2 rad.    3π/4 rad.    π rad.

(b) RCP ($\sigma = -1$), $l = -2$ @686 nm

0 rad.    π/4 rad.    π/2 rad.    3π/4 rad.    π rad.

(c) RCP ($\sigma = -1$), $l = -3$ @638 nm

0 rad.    π/4 rad.    π/2 rad.    3π/4 rad.    π rad.

(d) RCP ($\sigma = -1$), $l = +3$ @782 nm

0 rad.    π/4 rad.    π/2 rad.    3π/4 rad.    π rad.

(e) LCP ($\sigma = +1$), $l = +3$ @638

Min

0 rad.    π/4 rad.    π/2 rad.    3π/4 rad.    π rad.
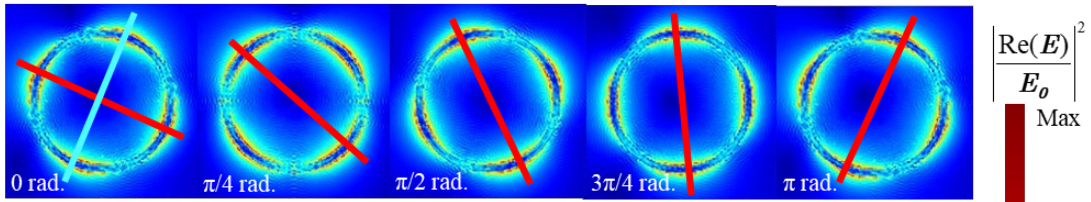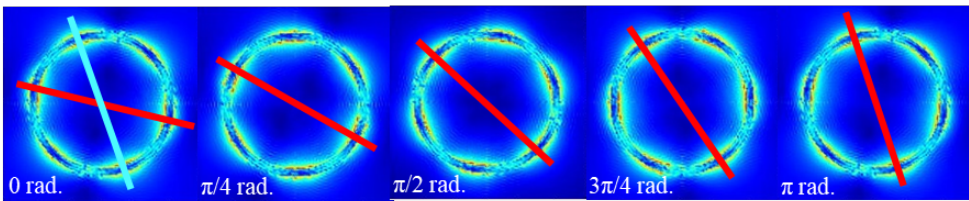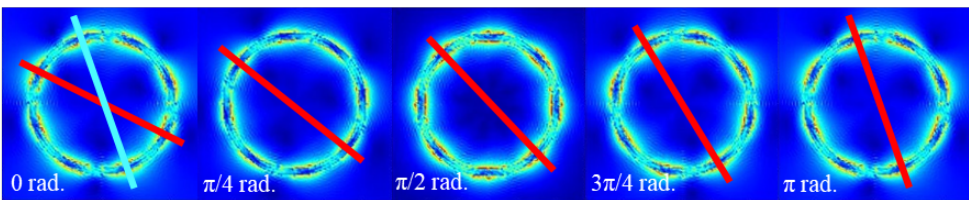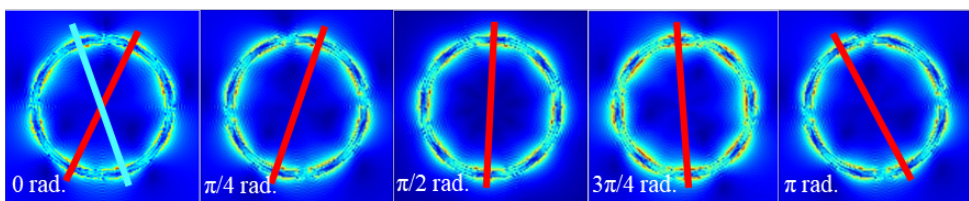
1
2
3
4
5
6
7
8
9
10

D. Tanaka et al. Figure 2

$l = -1$, RCP     $l = -2$, RCP     $l = -3$, RCP     $l = -4$, RCP

$l = -1$, LCP     $l = -2$, LCP     $l = -3$, LCP     $l = -4$, LCP

Extinction — Wavelength (nm)

B

@781 nm

0 rad.     $\pi/4$ rad.     $\pi/2$ rad.     $3\pi/4$ rad.     $\pi$ rad.

Max

Min

D. Tanaka et al. Figure 3
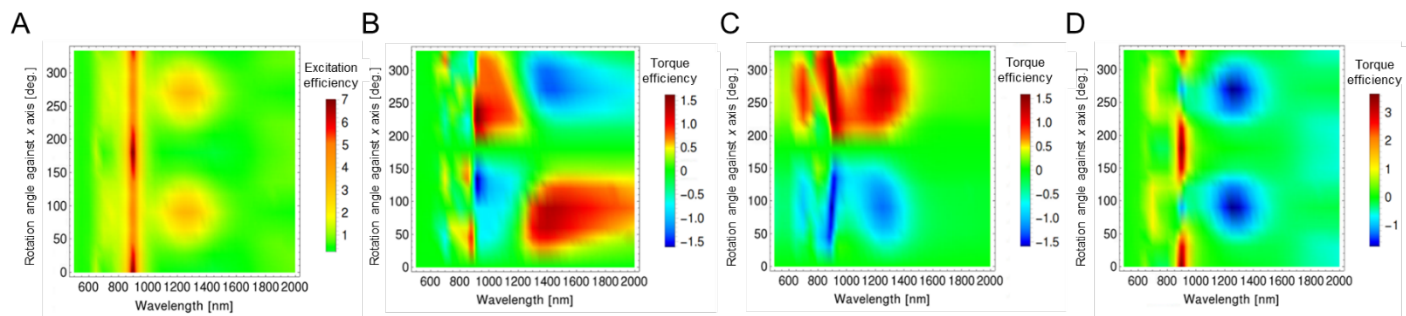
1
2
3
4
5
6
7
8
9
10
11
12
13
14
15
16
17
18
19
20

A



B
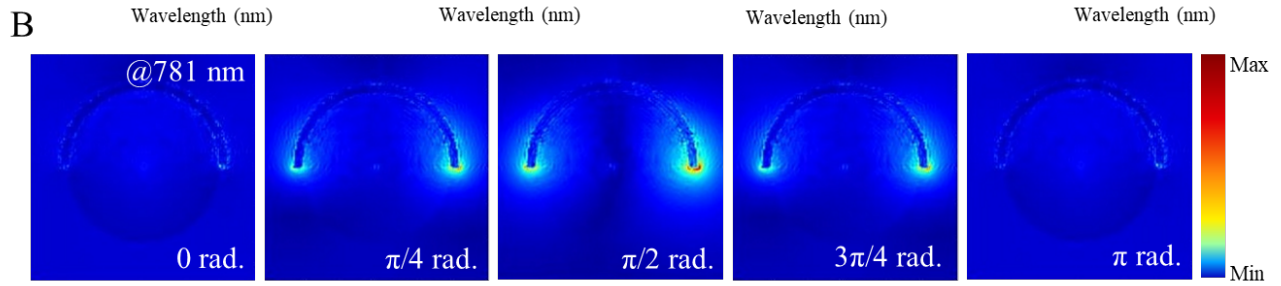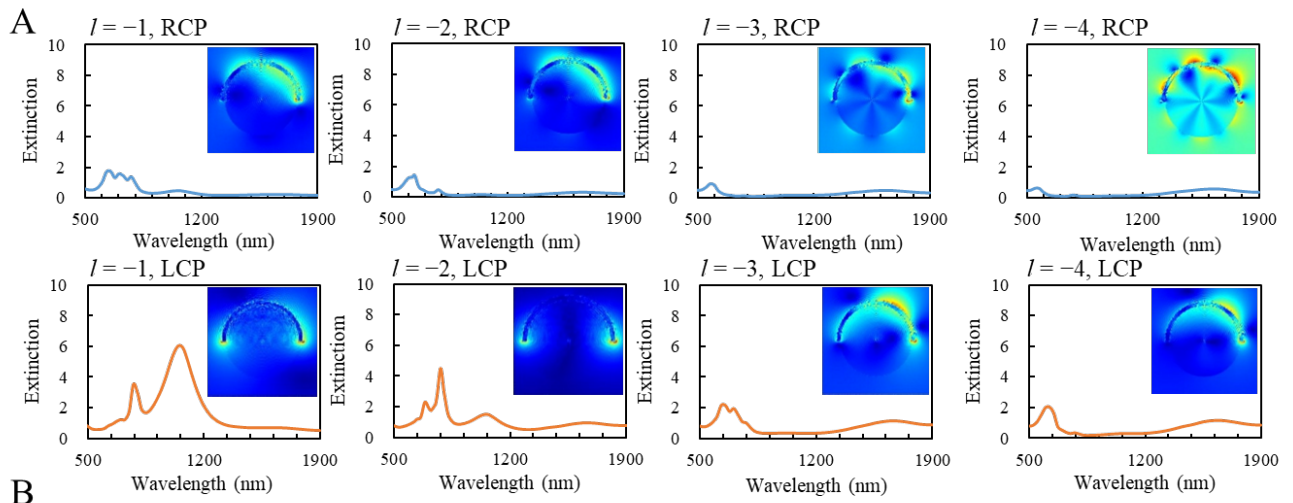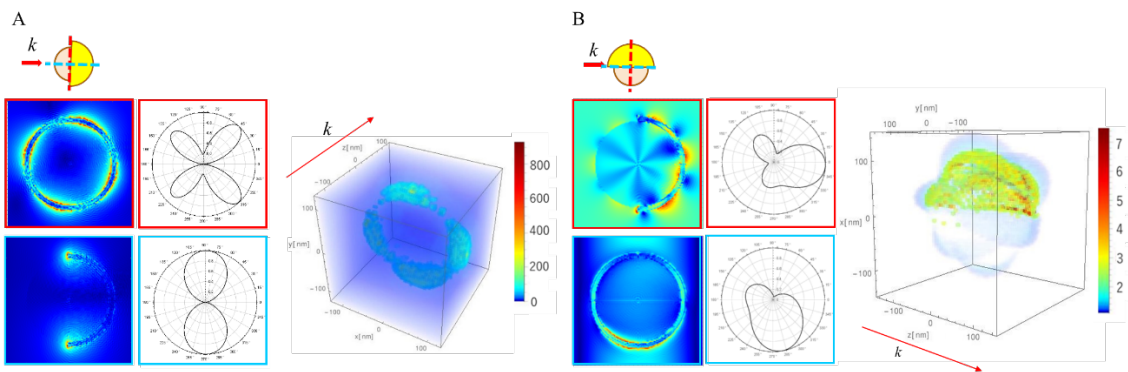


D. Tanaka et al. Figure 4

1
2
3
4
5
6
7
8
9
10
11
12
13
14
15
16
17
18
19
20
21
22
23
24
25
26
27
28
29

A    B    C    D

D. Tanaka et al. Figure 5

1
2
3
4
5
6
7
8
9
10
11
12
13
14
15
16
17
18
19
20
21
22
23
24
25
26
27
28
29